Large-Area Arrays of Quasi-3D Au Nanostructures for Polarization-Selective Mid-Infrared Metasurfaces

Vivek Nagal[1], Tengfei Li[2], Jacob B. Khurgin[2,], David H. Gracias[1,3,4*] (dgracias@jhu.edu)*

[1]Department of Chemical and Biomolecular Engineering and [2]Department of Electrical Engineering, [3]Department of Materials Science and Engineering, [4]Department of Chemistry, Johns Hopkins University, Baltimore, Maryland 21218, United States

KEYWORDS: metamaterials, nanoimprint lithography, FTIR, surface plasmon resonance, plasmonics

ABSTRACT

Metasurfaces are two dimensional patterns that are used to manipulate the propagation of light by controlling the resultant transmittance, reflectance, or absorption at specific wavelengths. Metasurfaces are typically composed of metallic or dielectric components arranged in single or multiple layers and with sizes significantly less than the wavelength of incident light. While considerable advances have been made in the design of these surfaces, there are significant challenges with high-throughput parallel fabrication over large areas which limits their applicability. Here, we demonstrate the design and characterization of mid-IR metasurfaces fabricated using a combination of photo and NanoImprint Lithography (NIL). We fabricate arrays over millimeter scales with a variety of 3D nanoscale designs including asymmetric disjointed shapes and symmetric accordion-like shapes with widths of 400 to 600 nm, thickness of 30 to 50 nm and lengths of 5 to 6 μm. We characterize the mid-IR optical response of these metasurfaces in reflection using Fourier transform infrared (FTIR) microscopy and simulate the spectral response using Finite element method (FEM) calculations with good agreement between simulations and experiments. Also, we demonstrate that the metasurfaces exhibit characteristic and significantly different plasmonic resonance modes based on the polarization of the incoming light. Our large area fabrication methodology allows cost-effective fabrication of large area metasurfaces with 3D micro and nanoelements for scalable photonic and plasmonic devices with significant tunability in geometry and optical characteristics.

1. INTRODUCTION

Conventional optical devices, based on light manipulation via accumulated propagation, through for the most part homogenous media, are inherently bulky and loss-intensive.[1,2] Hence, recent efforts have been directed at miniaturization and integration with modern photonic techniques.[3] One of the most promising directions is metamaterials which are three-dimensional artificial materials that can manipulate the propagation of electromagnetic[4] or sound (acoustic) waves,[5,6] and can benefit communication, imaging, sensing, and energy harvesting.[7] Typically composed of periodic patterns of metal, dielectric,[8] or a combination of metal-dielectric structures,[9,10] 3D metamaterials enable tunability of the effective permeability, permittivity,[11] extinction parameters,[12,13] frequency[14] and hence the spatial distribution of the wave response. Thereby, one can realize optical phenomena such as asymmetric transmission, [8] polarization control,[15] absorption/emission management,[16,17] negative refraction,[18] super resolution imaging,[19] and even electromagnetic invisibility.[20] However, there are significant challenges for large scale fabrication and reducing electromagnetic losses of fully 3D metamaterials.

For these reasons, in the last decade, the emphasis of the research has shifted towards metasurfaces, which are inherently two-dimensional (2D) metamaterials, composed of monolayer or few-layered planar stacks that offer same functionality as bulk metamaterials but in a more compact, lighter and loss-efficient manner (lower Q-factors).[21] Factors like the choice of materials, number of layers, and geometry facilitate tunability in their spectral response to realize characteristics like selective reflection and transmission along with phase control.[1,3,22] Metasurfaces can even manipulate light in more complex ways in 3D to create broadband circular polarizers,[23] quarter wave plates,[24] helical phase beams,[25] and computer generated holograms.[26]

As compared to fully 3D metamaterials, a major advantage of metasurfaces is that they are compatible with conventional optoelectronic chips and are easier to fabricate as most lithographic patterning techniques are inherently planar. With metal, dielectric, and semiconductor building blocks at their core, metasurfaces can be patterned and integrated using wafer-scale techniques.[27] This key feature is critical to advance practical use of this promising technology in smart nanophotonic and optoelectronic devices.[28]

For metasurfaces of relevance to visible and infrared (IR) devices such as antenna sensing,[29,30] spatial and spectral emission control,[31] perfect absorption via selective narrow-band and dual-band emission,[32] radioactive cooling via solar reflectors[33] and label-free analyte-sensitive biosensing using multi-resonant responses,[34] there is a prerequisite for highly parallel sub-micron patterning over large areas. Currently, most devices are fabricated using Electron-Beam Lithography (EBL) or Focused-Ion Beam lithography (FIB).[9,35] EBL and FIB offer high resolution but are serial techniques with relatively low throughput and high cost. In contrast, nanoimprint lithography (NIL)[36] which uses stamps and molds allows high fidelity parallel patterning using with resolution as low as 10 nm. Like photolithography, NIL also allows repeated replication of nanoscale patterns over larger areas as the stamps and molds are reusable. Unlike photolithography, NIL relies on the thermo-mechanical deformation of polymer resists and consequently the resolution of NIL is not limited by diffraction.

NIL has previously been used to fabricate metamaterials and metasurfaces to achieve different predictable photonic effects. Initially, NIL was predominantly used to exploit the localized surface plasmon resonance (LSPR) and ensemble electron density oscillations observed in noble metal nanoscale patterns.[37] Subsequently, NIL was also used to create plasmonic waveguides either planar ones on thin metal strips[38,39] or over profiled metal surfaces.[40,41]

Experimental realizations for a wider range of wavelengths have also been realized. For example, Wu et al.[42,43] reported fabrication of a mid-IR metamaterial and Yao et al[44] fabricated a large area metasurface with stacked subwavelength gratings and observed asymmetric transmission response with superior extinction in visible to mid IR range. NIL has even been creatively used in derived forms, such as to make exotic multilayer structures based on a stacking process to demonstrate negative index 'fishnet' and 'Swiss-cross' metamaterials.[45] Another such variant is soft UV-NIL where the soft polymeric stamp is transparent and in contact with UV-curable resist in absence of external pressure. This method was used to make 2D nanocavities for biosensing with near perfect absorption capability in the near IR.[46] A similar fabrication methodology was used to make cylindrical nanowells for LSPR sensing and SERS (Surface Enhanced Raman Scattering) substrates.[47] With the aid of angled deposition, elliptical gold nanodisks were realized for clinical immunoassay[48] which highlights the geometric adaptability of NIL.

Direct nanoimprinting on metallic films[49] or nanoparticles[50] has also been previously utilized to manufacture plasmonic nanostructures with strong SERS effects and highly sensitive LSPR sensing arrays respectively. Using colloidal gold nanocrystal based nanoantennas patterned using NIL, Chen et al.[51] demonstrated an ultrathin polarizing plasmonic metasurface and a quarter wave plate. Similar devices when used with a hydrogel layer on top serve as an angle independent optical moisture sensor.[52] More recently, Park et al.[53] patterned Fe/Al_2O_3 films via NIL to engineer the modulation of effective density and refractive index of CNT (Carbon Nanotube) forests. These examples highlight the compatibility of NIL with diverse types of metallic and non-metallic materials. The rationale behind our work was to further extend the adaptability of using NIL for more curved, complex and 3D topographies (like a hook or accordion) that offer-device grade optical functionality.

Here, we report the design and characterization of mid-IR metasurfaces fabricated using NIL coupled combined with conventional photolithography. Our metasurfaces consist of sub-micron periodic antenna units with selective dual band spectral responses in the wavelength brackets 4-6 μm and 10-15 μm. We were motivated to mass produce mid-wave IR (MWIR) responsive metasurfaces for several reasons. First, the atmosphere is transparent in two mid-IR windows[54,55] due to minimal vibrational and rotational absorption of atmospheric gases such as oxygen and carbon dioxide.[56] Consequently, signals in the mid-IR are widely used for environmental and remote sensing.[57] Second, commonly encountered thermal emissions from humans and hot objects such as aircraft engines correspond to temperature ranges of 300 to 1000 K in the MWIR band.[58] Thus MWIR metasurfaces have potential applications in energy harvesting, tracking, camouflaging, and ambient radiative cooling. Conventional MWIR optics for such applications are bulk and expensive. Finally, the losses in metallic metasurfaces are lower in the MWIR range as compared to shorter wavelength regions such as the visible and near IR. We note that NIL allows us to create features on the order of several hundred nm which is commensurate with the subwavelength size and periodicity of 'meta-atoms' in the MWIR range.

We utilize a comprehensive approach for design and prediction of the optical responses for various antenna shapes and sizes in the mid-IR wavelengths using numerical simulations in COMSOL. Using the fabrication protocol described in subsequent sections, we reproducibly create metasurfaces over millimeter-sized areas using NIL and measure the optical responses using Fourier transform infrared (FTIR) microscopy. We observed good agreement between simulations and experiments. The results demonstrate the versatility of the method for two different types of metasurfaces: disjointed-hook (DHM) and accordion-like (ALM).

2. METHODS

2.1 Large area nano-patterning of metasurfaces: Fabrication details are illustrated in **Fig. 1.** We first spin coated a thermally curable resist NXR-1025 (7%, Nanonex Corp) at 2000 rpm and baked the resist at 115°C for 1 minute. We stamped the wafer using a commercial NX-2000 imprinting tool with an 8 x 8 mm^2 mold (LightSmyth) with the nanolines feature. We performed stamping via a controlled cycle with an applied peak pressure of 200 psi and peak temperature of 120°C. We loaded the resulting samples in a dry planar etcher with 22 sccm oxygen flow at 100W RF power for a minute to reach the bottom of the substrate as shown in **Fig. 1** (D). Next, using thermal evaporation in tungsten boats, we deposited (5-10 nm) adhesive layer of chromium followed by 30 - 50 nm thick gold film at a deposition rate of 0.1 – 1 Å/sec in 1 x 10^{-5} Torr chamber pressure. After this step, we dissolved the residual imprint resist in acetone for lift-off metallization using a sonication bath. These steps define the width of the nanoantennas.

In order to fabricate nano-antenna units from the NIL patterned nano-lines, we spin coated a UV-curable photoresist S1805 by Microposit at 4000 rpm and then baked it at 115°C for 1 minute. I-line (365 nm) exposure was done using a Neutronix NXQ 4000 mask aligner and the resist was developed using MF-319 developer for 7 sec. The photopatterning alignment was done such that the micron-sized periodic line pairs on the chromium photomask were orthogonal to the imprinted gold lines, hence this step determined the final length of our antennas. The unmasked gold regions between any two resist line pairs were dissolved at room temperature using a commercially purchased wet etchant GE-8110 (Transene). The chemistry was selective towards gold with an added surfactant to enhance the wetting. Chromium etchant CR 1020 AC (Transene) was applied to remove the underlying chromium below the gold removed. Eventually, the resist

was washed off using acetone to give rectangular cantilever-shaped antennas. The aforementioned protocol for making single layer metasurfaces can be adapted for MIM (metal-insulator-metal) structures with the addition of two preceding steps as shown in **Fig. 1** (A). First, was thermal evaporation of the back reflector metal layer with a thickness of approximately 200 nm, followed by a subsequent deposition of the 120 nm thick dielectric spacer layer, which was magnesium fluoride (MgF_2) for our study.

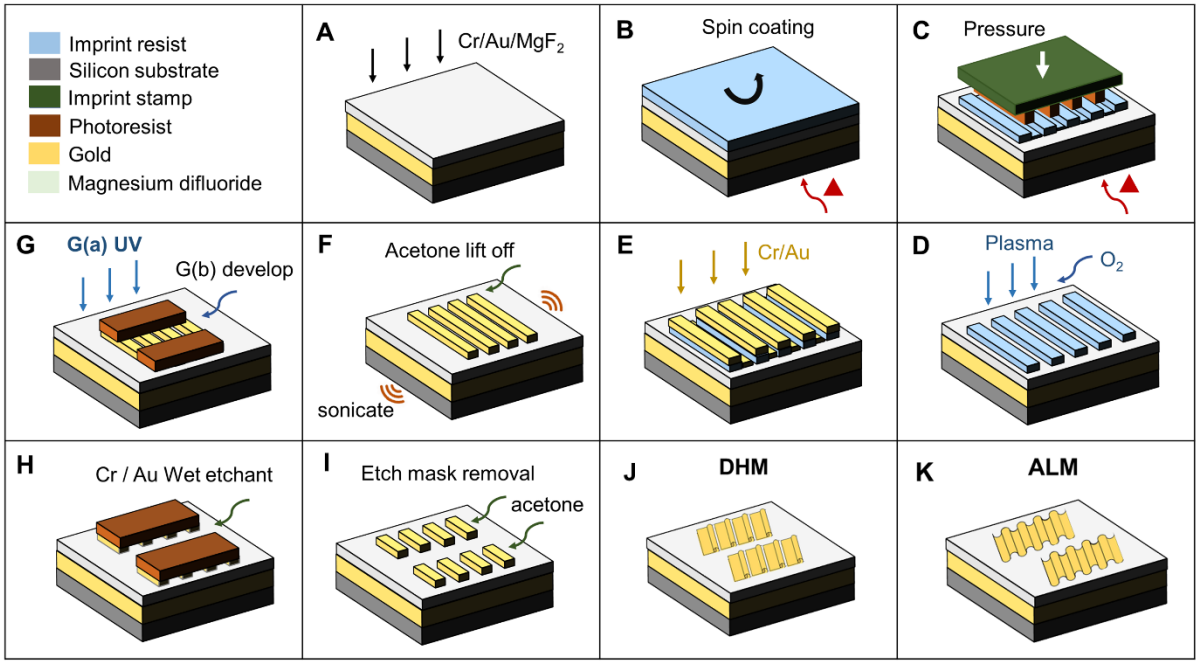

Figure 1: General fabrication process for both metasurface types. **a)** Thermal deposition of Au followed by MgF_2 onto the silicon substrate. **b)** Spin coating of the thermoplastic resist on top for the imprint process. **c)** Pressure and temperature-controlled NIL step under vacuum to transfer the nanolines. **d)** Removal of the residual resist after NIL using an oxygen plasma descum to reach the substrate. **e)** Thermal deposition of the Au desired thickness preceded by deposition of an adhesive layer of Cr. **f)** Lift-off metallization by sonication in an acetone bath to remove the resist. **g)** Photopatterning of the resist etch mask perpendicular to the direction of the imprinted lines followed by developing to expose the unwanted Au. **h)** Wet etching of the Au followed by Cr using commercially available selective etchants. **i)** Removal of the etch mask resist layer using acetone. **j)** Image of the disjointed hook metasurface (DHM). **k)** Image of the accordion-like metasurface (ALM).

2.2 Fabrication variation of DHM and ALM: The main difference in the fabrication methodology of the DHM and ALM occurs during the steps D and E explained earlier in **Fig. 1**.

Given the nanolines in our commercially procured stamp, the resulting resist side profile is as shown in **Fig. 2** A (i) alongside a representative schematic A (ii). During the deposition of gold in a vacuum chamber, the DHM and ALM are obtained from different positions on the substrate holder plate as shown in schematic B (i). The solid angle projected by the gold target below resulted in a normally incident vapor flux for the ALM as seen in schematic B (iii). Whereas for the DHM, the deposition of top gold layer occurs at an angle due to the shadow effect[59, 60] casted by the solid angle of gold flux as shown in panel B (ii), thereby ensuring the discontinuity in the film. Once the acetone lift-off is performed (step F in **Fig. 1**), the ALM is realized directly as seen in panel C (iii), while the antennas in DHM undergo slight curvature shown by the hook topography in schematic C (ii). We hypothesize that this curving occurs due to the differential stress in the Cr/Au bilayer, which when released from the contact with the imprint resist, relaxed to an unstressed state. The direction of this minimal bending is downwards towards the substrate given the higher stress in Cr layer than the Au layer.[61] This outcome is realized in the SEM of DHM in panel C (i). In this paper, as a proof-of-concept, we explored the two limiting cases, when the substrates are towards the center and at the edge of the holder plate during deposition.

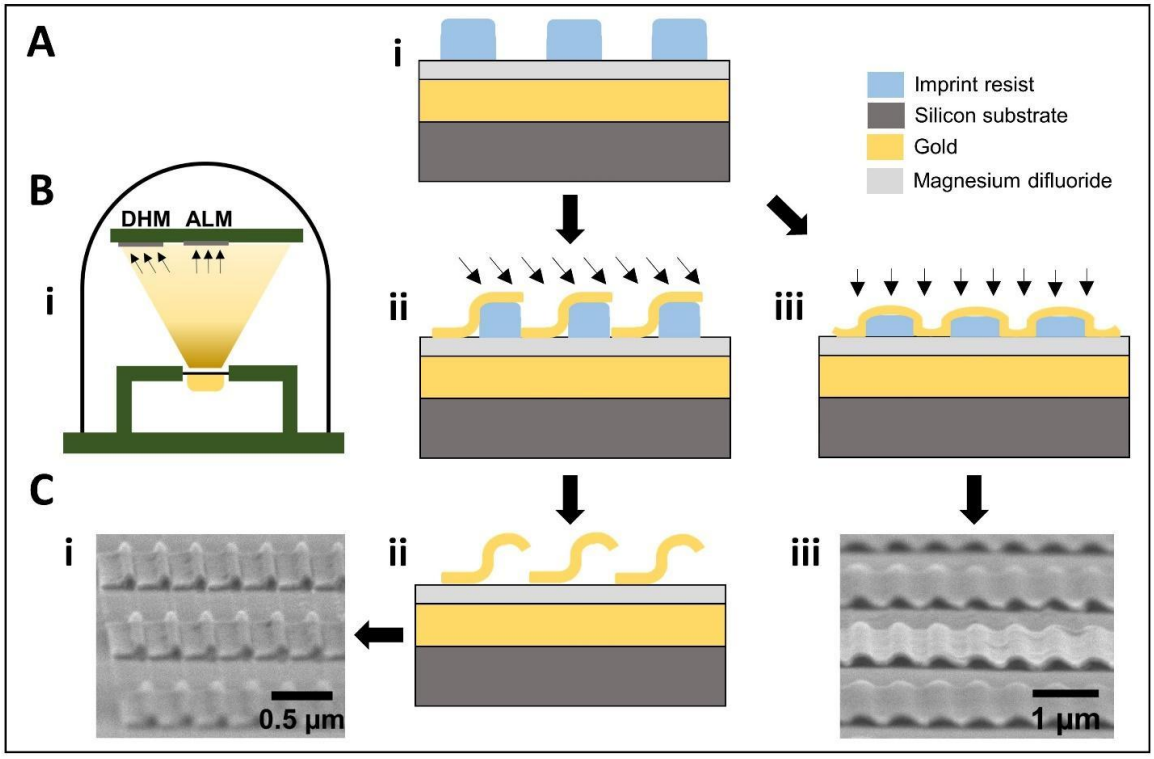

Figure 2: Obtaining DHM and ALM: (A) (i) schematic representation of sample side profile of imprint resist lines MIM substrate after NIL using one of our stamps for metasurface fabrication; **(B) (i)** Schematic representation of vacuum chamber for gold thermal deposition with arrows representing the incoming vapor flux from gold target below; **(ii)** which is at an angle for the DHM; **(iii)** and normally incident for the ALM during the evaporation step. **(C)** SEM micrograph of the resulting **(i)** DHM and **(iii)** ALM; **(ii)** schematic showing that post the lift-off step, the antennas in DHM undergo small degree of bending due to release of differential stress in the Cr/Au bilayer to generate the hook topography.

2.3 Fourier Transform IR Characterization: We performed the reflectance measurements for our metasurfaces using a Bruker Tensor 27 FTIR spectrometer coupled to a Hyperion 2000 microscope. We focused the incident light from the source on the sample using a 15X visible-cum-IR objective (NA = 0.4) and collected it back using a liquid nitrogen cooled mercury cadmium telluride (MCT) detector. The weighted average angle of incidence for reflection measurements was 20°. We used the reflection spectrum from a gold mirror to normalize all sample reflection spectra. We confined the collection area to $100 \times 100\ \mu m^2$ by a rectangular glass aperture to consider a region with minimal defects. We placed an IR polarizer in the path of

incident light before it hit the sample, at two optional angles of 0° and 90° to generate linearly polarized light with parallel and perpendicular states with respect to the antenna. We did not use an analyzer for the resulting light off the metasurface. We collected spectra for the samples and background from 2 to 16 μm at a resolution of 1 cm^{-1} containing 64 scans with a mirror repetition rate of 20 kHz. We corrected the spectra using the atmospheric compensation tool (for H_2O and CO_2) in OPUS package by Bruker and post processed for smoothening by Savitzky-Golay algorithm.

2.4 FEM Modelling: We explored a number of complex geometries in COMSOL Multiphysics® using the electromagnetics module to mimic the shape of the antennas in both types of metasurfaces. In order to accurately capture the curvature nuances of our metasurfaces, we used basic geometric modelling to approximate the unit cell input for setting our FEM calculations in COMSOL based on the ImageJ characterization of SEM micrographs as shown for DHM in Fig. S3. The details of these mathematical design paradigms are described in more detail in the supporting info section 1 (Fig. S1 and S2). We simulated unit cells with boundary conditions in the x and y direction as infinitely large periodic area. We used the light source as a plane wave and calculated the reflection, transmission and absorption during the simulations by setting frequency-domain power monitors. We used literature values for the optical parameters of Au[62] and MgF_2.[63] The light was incident through the period port and we obtained the reflection via S-parameters.

2.5 Design Considerations: We used undoped <100> high resistivity (>10, 000 ohm-cm), 525 (±10) μm thick silicon wafer as the substrate in both the metasurfaces. We used float zone grade silicon, which is usually used to fabricate optical components in the semiconductor industry and single side polished wafer for our reflection measurements. As compared to low resistivity

counterparts, our high resistivity silicon substrates show better mid IR performance for mid IR wavelengths. We farbicated the MIM assembly from the Au-MgF_2-Au trio. Based on our predictions of real and imaginary parts of the dielectric constant for mid-IR wavelengths (see supporting info Fig. S4) of the three most commonly used plasmonic materials: Au, Ag and Cu, we chose Au. Regarding another prospective choice: Al as a plasmonic material (as well a reflective material) is mainly applicable in the blue and UV regions of spectrum. Ag, Cu and Au are strongly absorptive due to intra-band absorption. In mid-IR, however the loss in aluminum is higher than in Au, Ag and Cu. MgF_2 is an inexpensive dielectric material widely used in conjunction with Au for MIM devices, and can be deposited thermally, hence our choice for the insulator layer. Owing to the low refractive index (around 1.40) and absorption capacity of MgF_2 for mid-IR wavelengths[64] and scattering possible with tightly packed array of well oriented gold nanopatterns, we hypothesized that our design would exhibit optimal efficacy for mid-IR operation.

According to the generalized Snell's law[65] customized and optimized for a specific purpose, reflection can be obtained using the MIM metasurface structure. Compared to the non-MIM structure, the nano-antenna array on the top surface can couple to its own dipolar image in the back-metal mirror,[66,67] and hence can achieve a phase coverage of 2π. Furthermore, metasurfaces based on MIM stacks can significantly increase the efficiency compared to the non-MIM ones which is usually 10%-20%.[68,69] In addition, to help realize high efficiency abnormal reflection, MIM based metasurfaces are also widely used for the research of frequency selective, perfect wave absorbers and thermal radiation devices in the mid-IR wavelength region.

In conventional antenna theory, especially for the radio frequency and microwave regimes, antennas are widely used for converting the electromagnetic radiation into localized energy and *vice versa*. Optical antennas or nano-antennas are the extension of the traditional antenna concept into the optical wavelength ranges. In designing traditional antennas, the length of antennas L are directly related to the wavelength of incoming or outgoing radiation. At optical frequencies, the radiation penetrates the metal and drive the conduction electrons into collective oscillation known as localized surface plasmon resonance (LSPRs). This gives rise to an alteration of the incident radiation pattern and striking effects such as the subwavelength localization of electromagnetic energy, the formation of high intensity hot spots at the nano-antenna surface. Meanwhile, due to the excitation of LSPRs, the incident radiation is no longer perfectly reflected from the metal's surface. So, like the traditional antenna, for a half dipole antenna, the length of the nano-antenna should scale accordingly.[70]

3. RESULTS

3.1 Morphology of DHM and ALM: Our fabrication procedure is highly scalable and extremely effective in creating differently sized antenna components by simply using molds and masks of varying lateral characteristics (duty cycle or period, line width, depth, angle of photopatterning). The SEM images in **Fig. 3** show the good imprint integrity (negligible residual layers) and high-fidelity patterns at the submicron scale over large areas as described in the schematic. The progressively zoomed micrographs specifically show a disjointed array of antennas that are asymmetric along their width (hook-shaped topography) with approximately 50 nm height, 490 nm wide and 5.5 μm long with a period of 510 nm along the width and 10.1 μm along the length. The non-continuity and thickness of gold antennas is critical in determining the LSPR

activity for this case as explained later. We used ImageJ to analyze the SEM images and generate geometrical measurements of the patterns as discussed in supporting info Fig. S3. Similarly, as shown in **Fig. 4,** we realized the symmetric 3D accordion antenna array. The high-resolution SEM images show that the antennas are connected uniformly along the longer edge.

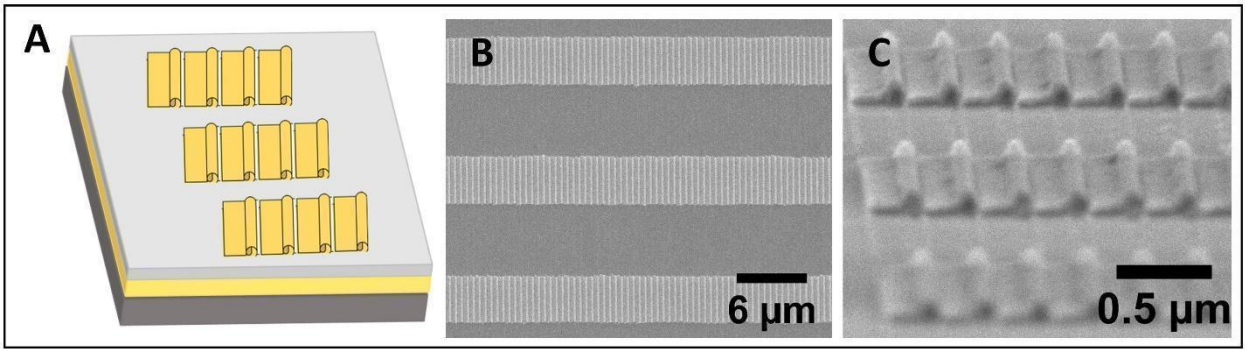

Figure 3: The disjointed hook metasurface (DHM). (A) Schematic of the DHM with the underlying silicon substrate, the thick metal layer, insulator layer and the disjointed hook-like gold nanopatterns. **(B)** Large area SEM micrograph of the DHM, and **(C)** zoomed-in SEM image with a tilted side view showing the novel hook topography of the individual antennas.

We realized high fidelity nanopatterning of the topmost gold antenna ensemble in both cases. We obtained a complex asymmetric topography in case of DHM over a large area as shown in panels B and C of **Fig. 3**. The antennas are separated along the right longitudinal edge and are closely packed adjacent to each other. In case of the ALM, we achieved a continuous periodic corrugation in the top gold layer and the surface profile is smoother for this case compared to DHM. A key visual cue that differentiates otherwise seemingly similar metasurfaces is that if one performs an asymmetric cross-sectional but periodic partitioning of the top gold layer in the ALM, we obtain the DHM topography. Hence, we can creatively exploit a simple and effective variation in lithography, described earlier in section 2.2 to fabricate tunable metasurfaces.

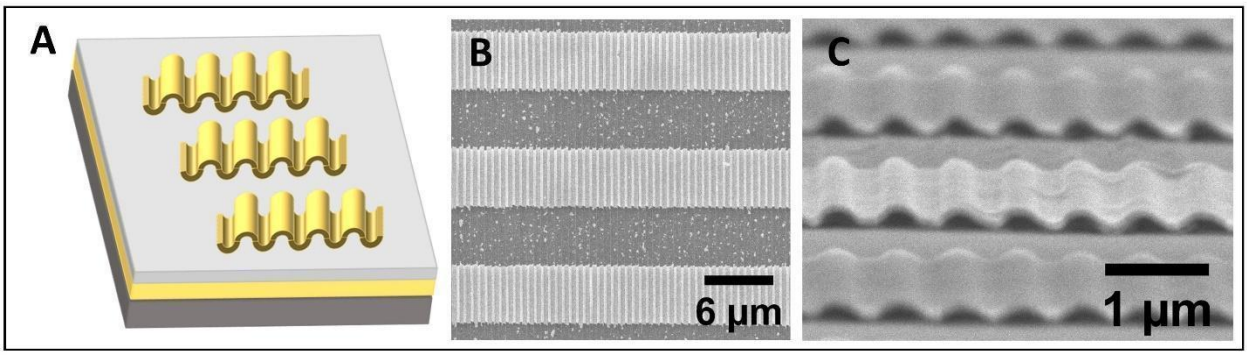

Figure 4: The accordion-like metasurface (ALM). (A) Schematic of the ALM with the underlying silicon substrate, the thick metal layer, insulator layer and accordion-like gold nanopatterns **(B)** Large area SEM micrograph of ALM, and **(C)** the zoomed-in SEM with a tilted side view to show the continuous connectivity of the antennas.

3.2 Surface plasmon modes in reflection spectra: The bottom gold layer in our metasurfaces was sufficiently thick to prevent through any transmission of incident light from above. Based on the electromagnetic resonance in the metal-insulator subwavelength bilayer, we saw reduced reflection for certain mid IR frequencies. We analyzed the reflection responses for three different cases and compared our results with the experimental measurements. **Fig. 5** and **Fig. 6** show simulated spectra from COMSOL in panels A, B and C and the FTIR measurements in panels D, E and F over the same wavelength range, for the DHM and the ALM respectively. The blue and the green curves denote the cases with incident light polarized along the longer and shorter edge of the antennas respectively, while the black curves are for unpolarized incident light. While it was experimentally possible to measure for all the three cases in our FTIR setup using an IR polarizer as described earlier in section 2.3, the FEM calculation for the no polarization case (panels A) was taken as a mean of the cases in panel B and C.

For the DHM, we observe significant reflection minima in the different mid IR regions at around 2, 5, and 12 μm. The responses near 5 and 10 μm result from the surface plasmon resonances along the longer edge of the antennas as realized in panels B and E of **Fig. 5** while the response at 2 μm is related to the plasmon resonance along the shorter edge of the antenna as seen in panels C and F of **Fig. 5**. For the ALM case, we observe the same resonances for wavelengths of 5 and 12 μm, with no discernable feature seen at shorter wavelengths lower than 1-5 μm. The

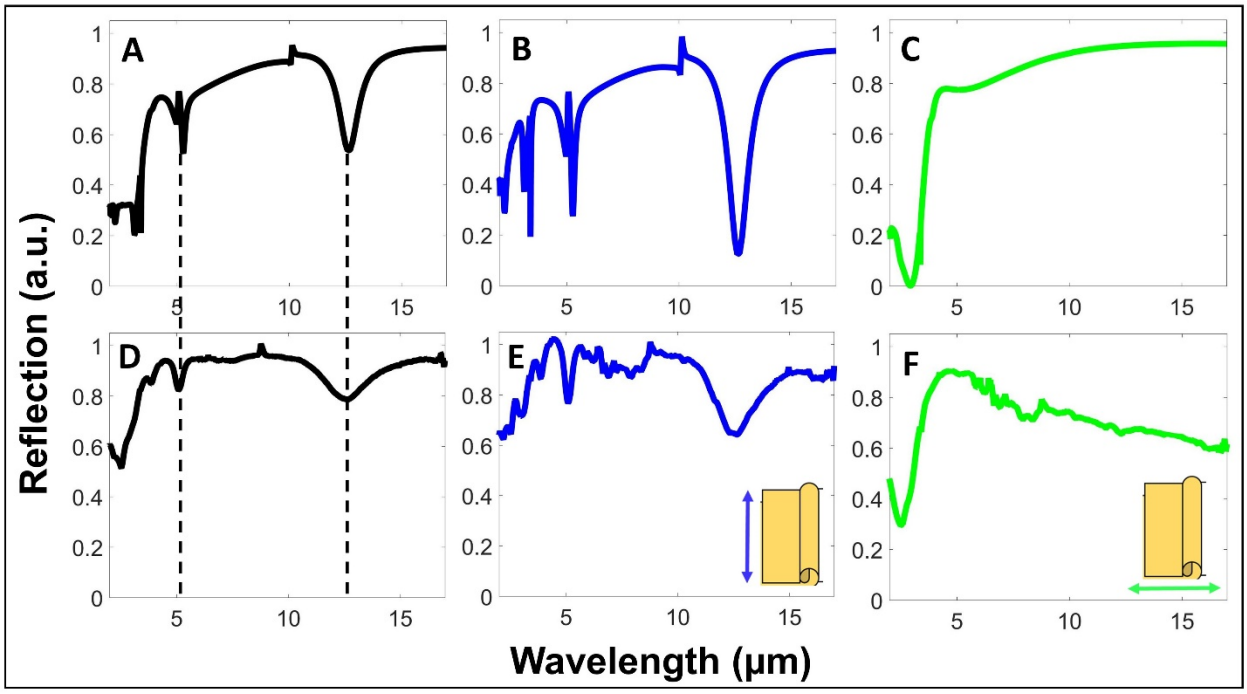

overall symmetric continuity of the structure along the shorter edge doesn't excite the same desired plasmonic interaction, as seen in DHM, to limit the reflection for higher frequencies as seen in green curves in panels C and F of **Fig. 6**.

Figure 5: Comparison of simulations and experimental FTIR spectra for the DHM. **(A-C)** FEM predictions in COMSOL for DHM described in **Fig. 3**. They are compared with **(D)** to **(F)** FTIR reflection measurements for the same cases represented by solid lines of same color. The IR polarizer used in experiments generated linearly polarized incident light at different angles with respect to the antenna, from **(D)** being no polarizer in beam path (black curve), **(E)** polarization along length of antenna (blue curve), and **(F)** polarization along the width of antenna (green curve).

All the LSPR interactions observed at different wavelengths in FTIR responses are largely consistent with the full wave simulations in the panels above of the same figures. For DHM, when light is polarized along the shorter dimension, the LSPR occurs at the highest energy (transverse) and conversely at the lowest energy (longitudinal) when light is polarized along the longer dimension. However, the same phenomenon is absent in ALM since antennas are connected to one another. This ability to differentiate between the two modes is possible with the orientation control given by NIL as opposed to the average of irregularly shaped structures that are chemically synthesized. This observation is in agreement with the reflection measurements in both cases where the blue curve (L pol) contributes to the main peak responses. The position of these

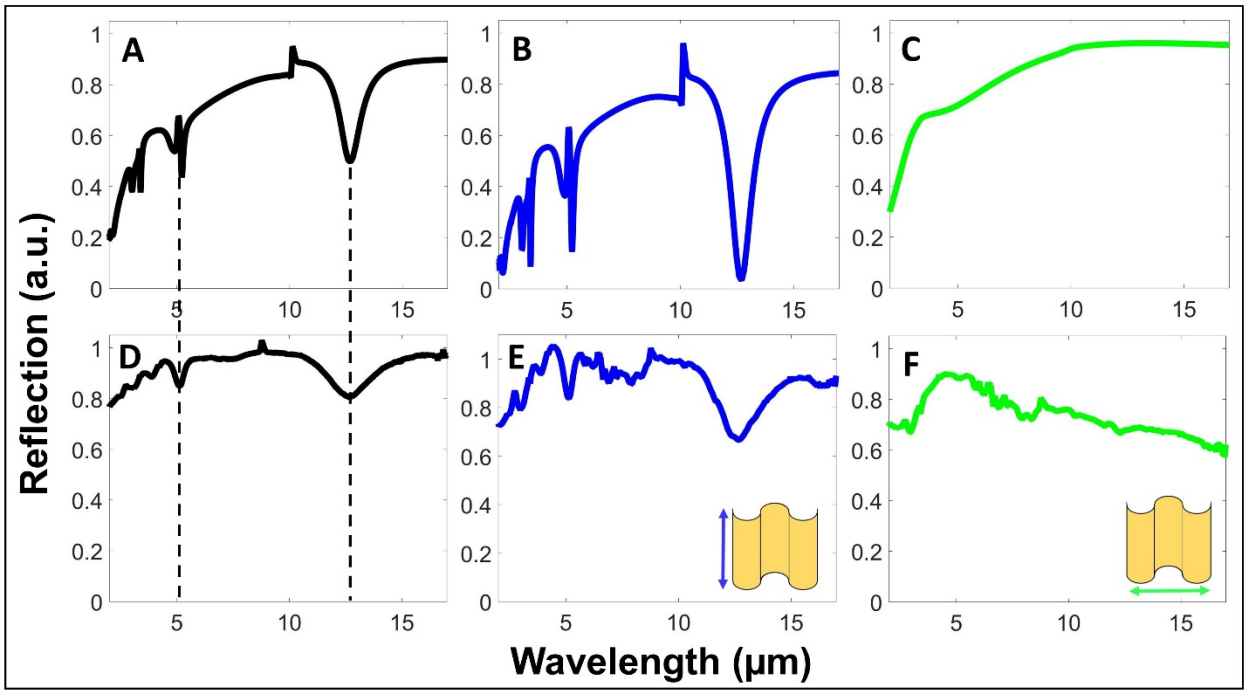

responses can be controlled and tuned using prefabrication changes. We also compared the reflection responses of metasurfaces in **Fig. 5** and **Fig. 6**, the reflection dip observed around λ = 2.5 μm for DHM is completely absent in the ALM. This shows that a simple change in the design can alter the optical nature of the said device from multi band to dual band response.

Figure 6: Comparison of simulations and experimental FTIR spectra for the ALM. (A-C) FEM predictions in COMSOL for ALM described in **Fig. 4**. They are compared with (**D)** to **(F)** FTIR reflection measurements for the same cases represented by solid lines of same color. The IR polarizer used in the experiments generated linearly polarized incident light at different angles with respect to the antenna, from **(D)** being no polarizer in beam path (black curve), **(E)** polarization along length of antenna (blue curve), and **(F)** polarization along the width of antenna (green curve).

3.3 Electric field intensity distributions of LSPR harmonics: In order to rationalize these symmetry and continuity driven reflection responses governed by LSPR interactions at the metal-dielectric interfaces, we also studied the electric field intensity distributions in the DHM and ALM unit cells. The intensity plots were calculated for different orders of LSPR as seen earlier in **Fig. 5** and **Fig. 6**. Within the mid-IR region, the first order being the higher intensity mode is located around 12 μm, the second order near 5 μm and the third at about 3 μm.

We observed that these SPP (Surface Plasmon Polaritons) modes are interfered with by three Fano resonances occurring at wavelengths 3.37, 5.08 and 10.13 μm and explained later in Fig. S5 of supporting text. Consequently, the second and third order SPPs are split into two different valleys each due to direct overlap with Fano resonances around those wavelengths. Hence, we explored the field intensity at 12.60, 5.28, 4.98, 3.39 and 3.12 μm for the DHM and at 12.71, 5.22, 4.93, 3.40 and 3.02 μm for the ALM, indicated by numerals, i, ii, iii, iv and v in panels A and B of **Fig. 7** and **Fig. 8** respectively, as described below.

The asymmetry in the DHM manifested itself in the hot spot locations of the resonances as shown in **Fig. 7** for the side view along length [panels A (i-v)] and the top view [panels B (i-v)] as encountered by incoming light. For the side view, the unit cell plane under consideration cuts the antenna on the right edge while the top view unit cell plane is at the mid-point of top antenna, parallel to the interface between top metal and underlying dielectric layer as explained in the inset

schematics (same holds true for **Fig. 8**). Therefore, for the top view in DHM we are looking at only the right half of field distribution. The said hot spots are shifted towards the right for the DHM, where the antenna rises in the out of plane direction. Juxtaposed against ALM, we saw more intense hot spots with ideal symmetry in the top view planes for all the orders [**Fig. 8** panels B (i-v)]. Given their smoother edgeless topography, the fields also extend further in the unit cell area under consideration than the DHM LSPR activity as seen from **Fig. 8** panels A (i-v). Hence, we can conclude that the geometric asymmetry in the DHM manifests itself in the hot spot locations of the resonances; likewise, symmetry played the same role in ALM.

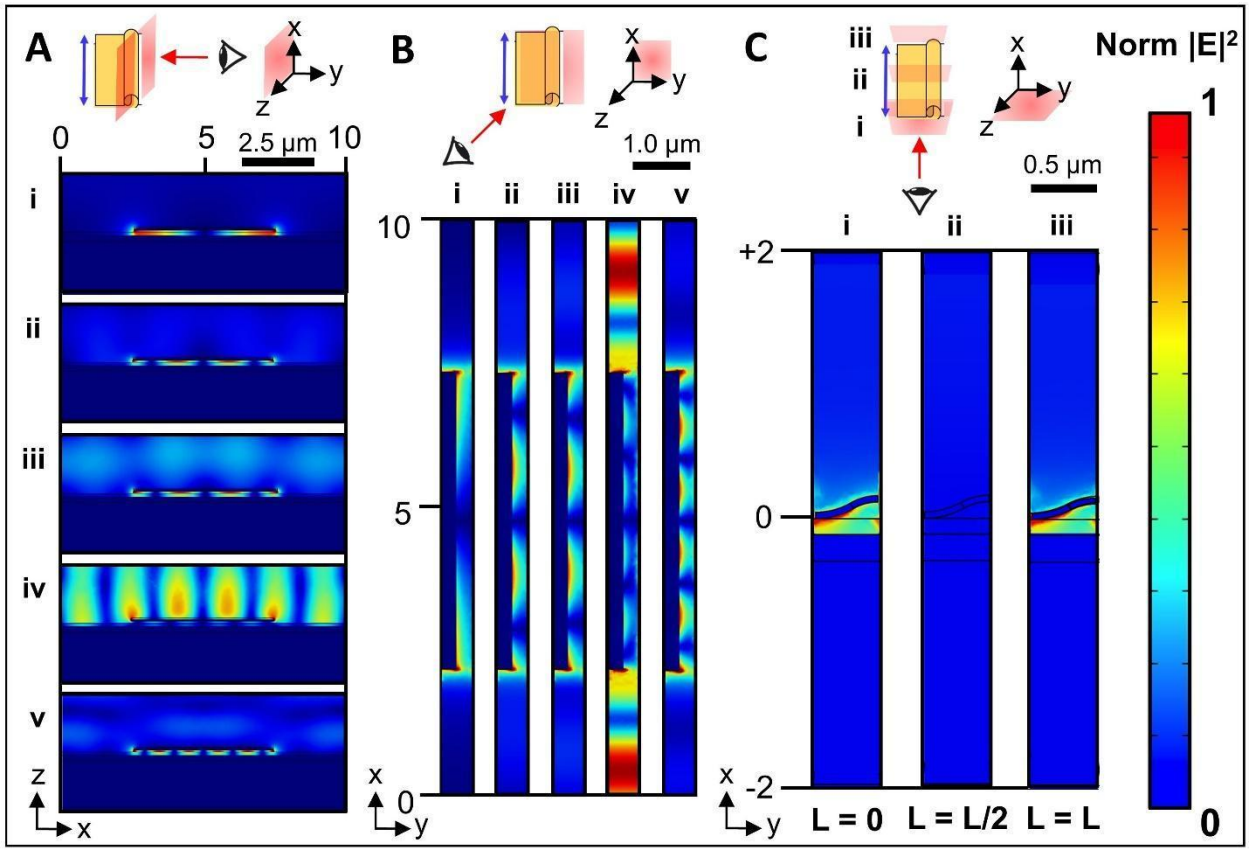

Figure 7: Electric field |E| distributions around the DHM unit cell: (**A**) (**i-v**) representing the SPPs observed in reflection response for increasingly blue wavelengths from top (**i**) to bottom (**v**) as viewed from the side projection in the x-z plane; **(B)** as viewed from the right half of top projection in x-y plane for same wavelengths respectively; and **(C)** shows the cross sectional view projections in y-z plane taken at 3 different levels: 2 ends of the antenna [**(i)** L = 0 and **(iii)** L = L] and one at the middle [**(ii)** L = L/2] for the

lowest order resonance seen. Top inset schematics indicate where the plane of interest meets the antenna for said cases.

More specifically to explore the plasmonic interactions taking place along the width of these antennas, where the difference in structural symmetry lies, we plotted the electric field intensity distribution for the longest wavelength (12 μm), evaluated at 3 different orthogonal planes: 2 at the edges [panels C (i, iii)] and one at the center [panels C (ii)] in both **Fig. 7** and **Fig. 8** as depicted by the inset schematic. We observed that the hot spots were realized at the edges in

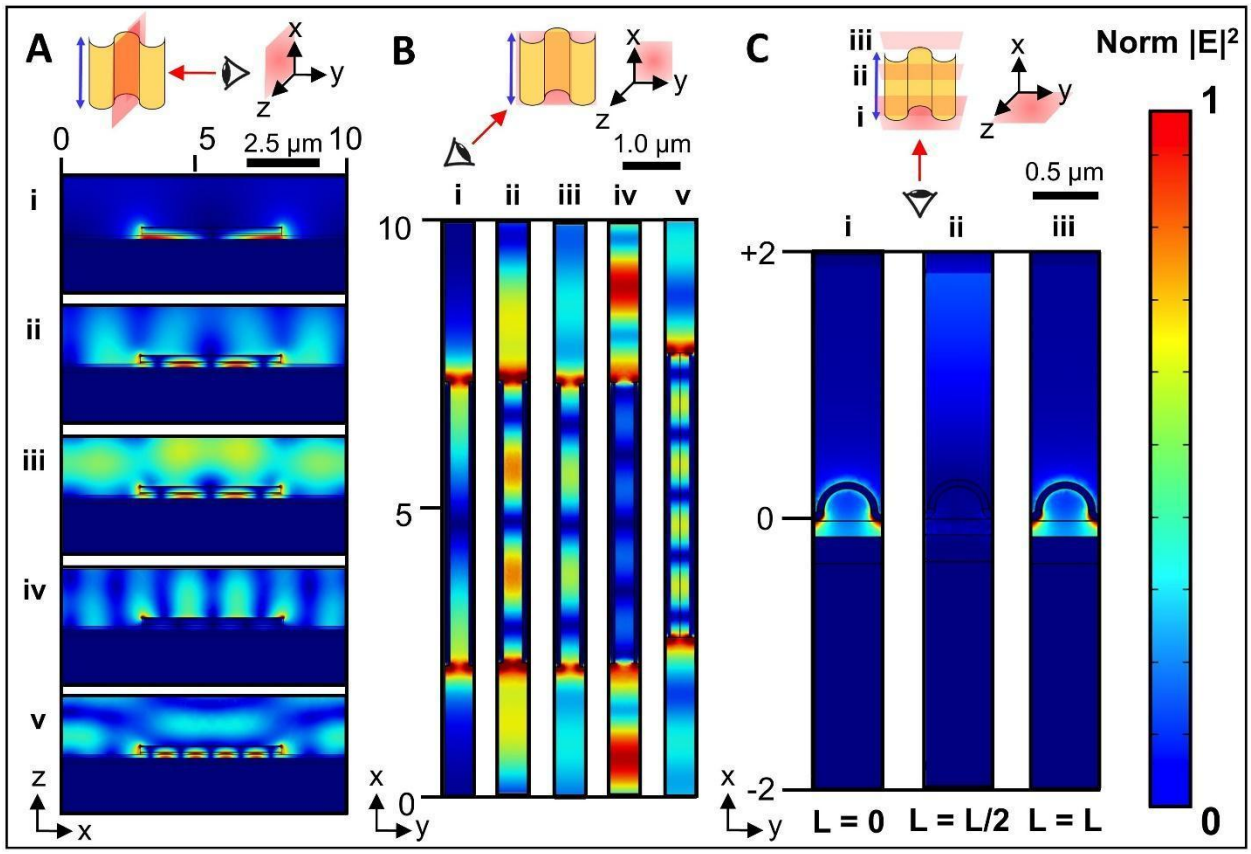

both cases, but in an asymmetric layout for the DHM as compared to a symmetric one for ALM. This observation establishes that the resulting distributions for the two cases are significantly different. In effect, using subtle symmetry manipulations in our metasurface fabrication we achieved contrasting plasmonic responses for reflected light.

Figure 8: Electric field |E| distributions around the ALM unit cell: (**A)** (**i-v**) representing the SPPs observed in reflection response for increasingly blue wavelengths from top (**i**) to bottom (**v**) as viewed from the side projection in the x-z plane; **(B)** as viewed from the central half of top projection in x-y plane for same wavelengths respectively; and **(C)** shows the cross sectional view projections in y-z plane taken at 3 different levels: 2 ends of the antenna [**(i)** L = 0 and **(iii)** L = L] and one at the middle [**(ii)** L = L/2] for the lowest order resonance seen. Top inset schematics indicate where the plane of interest meets the antenna for said cases.

4. DISCUSSION

In general, we observed good agreement in the profiles of FEM and FTIR for both DHM and ALM in terms of positions of band responses and baseline trends. There are a few disagreements present but we have sufficient insights to rationalize them: (i) the overall noise in FTIR measurements is higher compared to their smooth FEM counterparts. This can be attributed to the ideal surface profiles constructed in COMSOL which can't be said for the experimentally fabricated metasurfaces. The process of thermally evaporating a dielectric material is susceptible to the grainy morphology of the resulting thin film. The resulting grains or cavities can contribute to both enhanced scattering and a more diffused reflection rather than specular in simulations. Experimental limitations consequently results in greater noise and (ii) low amplitude response since a lesser relative intensity of light is interacting with the metasurface compared to the simulation unit cell. The FTIR reflection data was corrected by a factor of two to take into account the 50% reduction in overall light intensity occurring due to presence of the polarizer in the beam path. Based on the refractive index modelling of MgF_2 in most commonly used commercial Maxwell solvers, which is reliably researched and reported only as far as 7 to 7.5 microns,[63, 71] for both ordinary and extraordinary rays, the experimental observation of increasingly lossy behavior

for higher IR wavelengths is not fairly captured in our FEM calculations. (iii) The latter resulted in an increasingly reflective trend for the region of 7 to 15 μm in contradiction with the FTIR measurements. The location of this cut-off wavelength can be accounted for by the vibrational mode phonon energy corresponding to MgF_6 octahedron building blocks in the material's structure.[72] (iv) Another factor that can contribute to the enhanced absorption for certain wavelengths in FTIR data is the fact that the series of fabrication steps employed in our recipe involves extensive use of various cleaning reagents, thermosetting polymers, silanizing agents, photo responsive resists and chemical etchants. Absorption by even trace residual amounts of such compounds, comprising an abundance of different bond energies present, can interfere with the LSPR interactions which is again not accounted for in the simulations. (v) Sharp Fano-resonant features are seen in both cases. (vi) Other minor disagreements between the simulations and experiments can be attributed to the imperfections or defects present on the sample. The alignment errors during photopatterning leads to non-orthogonal antenna profiles along the width compared to perfect ideal geometry in COMSOL unit cell. (vii) For our reflection measurements, the concealing is achieved via a rectangular glass aperture, which can contribute to a more dispersive signal nature from interaction of light with its edges with an already reduced light intensity at play. Hence potentially by removing the microscope, and using the spectrometer alone to create a less angularly dispersive optical setup (like the one reported previously)[73] could enhance the signal quality. (viii) The experimental measurement conditions (not in vacuum) were different from the ideal simulation. With the use of Cassegrain objectives for FTIR microscopy, the reflected light can never be perfectly normal to the substrate as in case of wave optics module in COMSOL. If additional resolution or finer resonances need to be resolved, optical arrangement as reported

previously in literature[74] can be utilized. However, our setup can still monitor a significant amount of reflected light and, therefore shouldn't alter our conclusion.

The reflection of the MIM structure that we examine in this paper is determined by several elements. Since, the electromagnetic resonance on the top antennas is excited by the external incident electromagnetic wave, both the size of the antenna and the polarization have an effect on the reflection spectrum. The bottom metal (Au) in the MIM stack acts as a mirror, which couples to the resonance of the top antenna, enhances the interaction, then both the distance between antenna and bottom metal and the material between them will impact the interaction. As a summary, by changing the size and polarization, we can change the resonance wavelength, hence the position where the trough in the spectrum shows. Because different resonance modes can be excited by the external incident electromagnetic, we can see that there are several dips in the spectrum. By changing the distance or the material between the top and bottom metal, we can change the depth of the trough of the spectrum, and potentially make the MIM structure a perfect absorber.

5. CONCLUSIONS

In summary, we realize large area nanomanufacturing of multilayer plasmonic metasurfaces using NIL and conventional photolithography. We note that, if needed, the wavelength response can be shifted to visible and near IR regimes when imprint stamps with features around 100 nm with varied packing density are used. We believe that the amplitude we achieved can be sufficient for biomolecular sensing applications and by altering the amount of plasmonic metal deposited, the intensity of the response can be also enhanced. When used in tandem with novel thermally, chemically or mechanically responsive materials or opto-

electronically relevant families of 2D layered materials, these metasurfaces can generate further exotic properties.

Overall, our work also demonstrates two subtly different metasurfaces with novel topographies operating in the mid IR region with highly tunable and complementary plasmonic responses sensitive to the state of linear polarization of the incoming light. To establish perspective towards the novelty of the 3D morphology aspect of these metasurfaces and how it affects the accompanying surface plasmonics, we can compare their reflection response towards polarized light in two different states (along the length and width of antennas) to the control cases where the antennas lack any apparent degree of patterning: a single continuous flat strip of gold [**Fig. 9** (A, E)] and non-corrugated rectangular cantilevers [**Fig. 9** (B, F)]. We only analyze the FEM reflection responses in COMSOL for this purpose. Since the location of plasmonic resonances on the reflection spectrum is determined primarily by the length of antenna, the blue curves (polarization along the length) generate a very similar outcome but with no significant attenuation seen in cases A and B. However, it is noteworthy to highlight the significantly different responses seen in green curves (polarization along the width). The changes in the overall intensity and peak position establishes the selective behavior of our metasurfaces towards polarization of incoming light.

Therefore, we believe these findings offer tremendous scope for exploring compact and tunable platforms for filters, wave-plates, and polarizers.

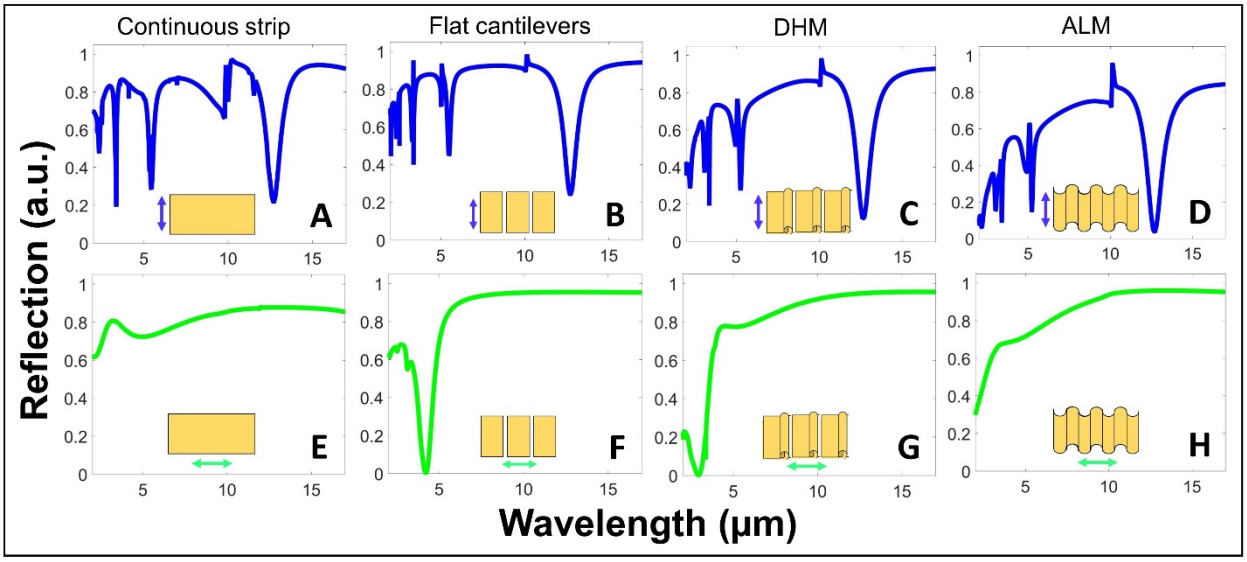

Figure 9: Comparison of simulated finite element reflection responses for the 2 indicated polarization cases (blue and green) with the respect to the antenna: **(A, E)** continuous single gold strip periodic in y-axis; (**B, F**) unpatterned rectangular gold cantilevers with perfectly flat and smooth topography, periodic along both x and y axis; (**C, G**) DHM and (**D, H**) ALM

By varying these asymmetric and symmetric nano-curvatures periodically over a large area of the semiconductor substrate, we are able to achieve true manipulation of possible IR responses on the spectrum scale indicated by easily distinguishable and unique plasmonic activity. This feature can be efficiently employed to accomplish otherwise esoteric tasks like accurate biosensing of molecules in low concentration or *in vivo* SERS, when the antennas are patterned to realize a plasmonic resonance that matches the energy transparency windows of the biological sample under consideration. Given the mid IR range of plasmonics in DHM and ALM (3, 5 and 12 μm) which overlaps with atmospheric transmission windows of 3-5 and 8-14 μm, we believe that they can be further adapted for developing solutions to enhance thermal cloaking and camouflaging as a function of controlled temperature and emissivity. It is noteworthy that the new dips in the reflection spectra (Fig. 9) correspond to peaks in the emission spectrum of the metasurfaces. This

feature combined with our ability for large area fabrication of such quasi-3D geometries opens up a significant new knob to tune the thermal signature of objects and use it, for example, for countermeasures.

We have discussed several shortcomings of the outcomes and offered recommendations to address them. Further experimentation is needed to fabricate more complex and truly 3D metamaterials by using these surface characteristics as building blocks arranged in polyhedral spatial fashion. We also anticipate that mounting the substrates at various inclined angles in path of the solid angle casted by metal flux from boat could lead to realizing intermediate nanostructures between DHM and ALM. Another parameter to vary is using different duty cycles in our imprints to achieve enhanced tunability. By varying the factors in the fabrication methodology, the desired resonances can be engineering to a reasonable extent. The materials and manufacturing techniques used in fabrication of these metasurfaces underline the compatibility with the semiconductor industry's conventional CMOS tech. Scalable and planar aspects of our device can comply with the increasing demand for miniaturization of optical components for compact portable device utilities, especially where on chip integrations are required. A significant portion of findings till date have heavily explored visible or near IR wavelengths, leaving out mid IR domain due to the lack of advanced nanomanufacturing methods and very expensive characterization techniques, and our research addresses these challenges and offers solutions with good agreement between experiments and simulations.

SUPPORTING INFORMATION

The Supporting Information is available free of charge at the ACS Publications Website

SI includes details on: Geometric designs for DHM and ALM; ImageJ analysis for dimensional characterization; Dielectric constant of different widely used metals; Comparison of overlapping

fano resonances; Comparison of polarization selectivity for 4 different cases (PDF)

AUTHOR INFORMATION

Corresponding Author

*Email: dgracias@jhu.edu; jakek@jhu.edu

Notes

The authors declare no competing financial interests.

ACKNOWLEDGEMENTS

We acknowledge support from the National Science Foundation (NSF); Division of Materials Research (DMR) - 1507749 and Division of Civil, Mechanical and Manufacturing Innovation (CMMI) – 1635443. V.N. would like to acknowledge the following personnel for insightful discussions and recommendations received during the course of this work: Dr. Lei Chen, Dr. Hye Rin Kwag and Dr. Edward Mertz.

REFERENCES

(1) Aieta, F.; Kats, M. A.; Genevet, P.; Capasso, F. Applied Optics. Multiwavelength Achromatic Metasurfaces by Dispersive Phase Compensation. *Science* **2015**, *347* (6228), 1342–1345.
(2) Khurgin, J. B.; Boltasseva, A. Reflecting upon the Losses in Plasmonics and Metamaterials. *MRS Bull.* **2012**, *37* (08), 768–779.
(3) Yu, N.; Capasso, F. Flat Optics with Designer Metasurfaces. *Nat. Mater.* **2014**, *13* (2), 139–150.
(4) Pendry, J. B. Controlling Electromagnetic Fields. *Science* **2006**, *312* (5781), 1780–1782.
(5) Liu, Z.; Zhang, X.; Mao, Y.; Zhu, Y. Y.; Yang, Z.; Chan, C. T.; Sheng, P. Locally Resonant Sonic Materials. *Science* **2000**, *289* (5485), 1734–1736.
(6) Cummer, S. A.; Christensen, J.; Alù, A. Controlling Sound with Acoustic Metamaterials. *Nature Reviews Materials* **2016**, *1* (3), 1-13.
(7) Holloway, C. L.; Kuester, E. F.; Gordon, J. A.; O'Hara, J.; Booth, J.; Smith, D. R. An Overview of the Theory and Applications of Metasurfaces: The Two-Dimensional Equivalents of Metamaterials.

IEEE Antennas Propag. Mag. **2012**, *54* (2), 10–35.
(8) Burckel, D. B.; Wendt, J. R.; Ten Eyck, G. A.; Ellis, A. R.; Brener, I.; Sinclair, M. B. Fabrication of 3D Metamaterial Resonators Using Self-Aligned Membrane Projection Lithography. *Adv. Mater.* **2010**, *22* (29), 3171–3175.
(9) Valentine, J.; Zhang, S.; Zentgraf, T.; Ulin-Avila, E.; Genov, D. A.; Bartal, G.; Zhang, X. Three-Dimensional Optical Metamaterial with a Negative Refractive Index. *Nature* **2008**, *455* (7211), 376–379.
(10) Liu, N.; Guo, H.; Fu, L.; Kaiser, S.; Schweizer, H.; Giessen, H. Three-Dimensional Photonic Metamaterials at Optical Frequencies. *Nat. Mater.* **2008**, *7* (1), 31–37.
(11) Veselago, V. G. Electrodynamics of substances with simultaneously negative values of σ and μ. *Sov. Phys. Usp.* **1968**, *10* (4), 509–514.
(12) Jain, P. K.; El-Sayed, M. A. Plasmonic Coupling in Noble Metal Nanostructures. *Chem. Phys. Lett.* **2010**, *487* (4-6), 153–164.
(13) Verellen, N.; Sonnefraud, Y.; Sobhani, H.; Hao, F.; Moshchalkov, V. V.; Van Dorpe, P.; Nordlander, P.; Maier, S. A. Fano Resonances in Individual Coherent Plasmonic Nanocavities. *Nano Lett.* **2009**, *9* (4), 1663–1667.
(14) Sievenpiper, D.; Zhang, L.; Broas, R. F. J.; Alexopolous, N. G.; Yablonovitch, E. High-Impedance Electromagnetic Surfaces with a Forbidden Frequency Band. *IEEE Trans. Microw. Theory Tech.* **1999**, *47* (11), 2059–2074.
(15) Gansel, J. K.; Thiel, M.; Rill, M. S.; Decker, M.; Bade, K.; Saile, V.; von Freymann, G.; Linden, S.; Wegener, M. Gold Helix Photonic Metamaterial as Broadband Circular Polarizer. *Science* **2009**, *325* (5947), 1513–1515.
(16) Hossain, M. M.; Jia, B.; Gu, M. Metamaterials: A Metamaterial Emitter for Highly Efficient Radiative Cooling (Advanced Optical Materials 8/2015). *Advanced Optical Materials* **2015**, *3* (8), 980–980.
(17) Zhai, Y.; Ma, Y.; David, S. N.; Zhao, D.; Lou, R.; Tan, G.; Yang, R.; Yin, X. Scalable-Manufactured Randomized Glass-Polymer Hybrid Metamaterial for Daytime Radiative Cooling. *Science* **2017**, *355* (6329), 1062–1066.
(18) Smith, D. R. Metamaterials and Negative Refractive Index. *Science* **2004**, *305* (5685), 788–792.
(19) Khorasaninejad, M.; Chen, W. T.; Devlin, R. C.; Oh, J.; Zhu, A. Y.; Capasso, F. Metalenses at Visible Wavelengths: Diffraction-Limited Focusing and Subwavelength Resolution Imaging. *Science* **2016**, *352* (6290), 1190–1194.
(20) Ni, X.; Wong, Z. J.; Mrejen, M.; Wang, Y.; Zhang, X. An Ultrathin Invisibility Skin Cloak for Visible Light. *Science* **2015**, *349* (6254), 1310–1314.
(21) Kildishev, A. V.; Boltasseva, A.; Shalaev, V. M. Planar Photonics with Metasurfaces. *Science* **2013**, *339* (6125), 1232009.
(22) Blanchard, R.; Aoust, G.; Genevet, P.; Yu, N.; Kats, M. A.; Gaburro, Z.; Capasso, F. Modeling Nanoscale V-Shaped Antennas for the Design of Optical Phased Arrays. *Phys. Rev. B: Condens. Matter Mater. Phys.* **2012**, *85* (15), 155457.
(23) Zhao, Y.; Belkin, M. A.; Alù, A. Twisted Optical Metamaterials for Planarized Ultrathin Broadband Circular Polarizers. *Nat. Commun.* **2012**, *3* (1), 1-7.
(24) Yu, N.; Aieta, F.; Genevet, P.; Kats, M. A.; Gaburro, Z.; Capasso, F. A Broadband, Background-Free Quarter-Wave Plate Based on Plasmonic Metasurfaces. *Nano Lett.* **2012**, *12* (12), 6328–6333.
(25) Niv, A.; Biener, G.; Kleiner, V.; Hasman, E. Spiral Phase Elements Obtained by Use of Discrete Space-Variant Subwavelength Gratings. *Opt. Commun.* **2005**, *251* (4-6), 306–314.
(26) Levy, U.; Kim, H.-C.; Tsai, C.-H.; Fainman, Y. Near-Infrared Demonstration of Computer-Generated Holograms Implemented by Using Subwavelength Gratings with Space-Variant Orientation. *Opt. Lett.* **2005**, *30* (16), 2089–2091.
(27) Boltasseva, A.; Atwater, H. A. Materials Science. Low-Loss Plasmonic Metamaterials. *Science* **2011**, *331* (6015), 290–291.
(28) Fan, P.; Chettiar, U. K.; Cao, L.; Afshinmanesh, F.; Engheta, N.; Brongersma, M. L. An Invisible

Metal–semiconductor Photodetector. *Nat. Photonics* **2012**, *6* (6), 380–385.
(29) Businaro, L.; Limaj, O.; Giliberti, V.; Ortolani, M.; Di Gaspare, A.; Grenci, G.; Ciasca, G.; Gerardino, A.; de Ninno, A.; Lupi, S. Mid-Infrared Nanoantenna Arrays on Silicon and CaF2 Substrates for Sensing Applications. *Microelectron. Eng.* **2012**, *97*, 197–200.
(30) Miyazaki, H. T.; Kasaya, T.; Iwanaga, M.; Choi, B.; Sugimoto, Y.; Sakoda, K. Dual-Band Infrared Metasurface Thermal Emitter for CO2 Sensing. *Appl. Phys. Lett.* **2014**, *105* (12), 121107.
(31) Makhsiyan, M.; Bouchon, P.; Jaeck, J.; Pelouard, J.-L.; Haïdar, R. Shaping the Spatial and Spectral Emissivity at the Diffraction Limit. *Appl. Phys. Lett.* **2015**, *107* (25), 251103.
(32) Liu, X.; Tyler, T.; Starr, T.; Starr, A. F.; Jokerst, N. M.; Padilla, W. J. Taming the Blackbody with Infrared Metamaterials as Selective Thermal Emitters. *Phys. Rev. Lett.* **2011**, *107* (4), 045901.
(33) Sun, K.; Riedel, C. A.; Wang, Y.; Urbani, A.; Simeoni, M.; Mengali, S.; Zalkovskij, M.; Bilenberg, B.; de Groot, C. H.; Muskens, O. L. Metasurface Optical Solar Reflectors Using AZO Transparent Conducting Oxides for Radiative Cooling of Spacecraft. *ACS Photonics* **2017**, *5* (2), 495–501.
(34) Rodrigo, D.; Tittl, A.; Ait-Bouziad, N.; John-Herpin, A.; Limaj, O.; Kelly, C.; Yoo, D.; Wittenberg, N. J.; Oh, S.-H.; Lashuel, H. A.; Altug, H. Resolving Molecule-Specific Information in Dynamic Lipid Membrane Processes with Multi-Resonant Infrared Metasurfaces. *Nat. Commun.* **2018**, *9* (1), 2160.
(35) Ni, X.; Kildishev, A. V.; Shalaev, V. M. Metasurface Holograms for Visible Light. *Nat. Commun.* **2013**, *4* (1), 1-6.
(36) Chou, S. Y.; Krauss, P. R.; Renstrom, P. J. Imprint Lithography with 25-Nanometer Resolution. *Science* **1996**, *272* (5258), 85–87.
(37) Lucas, B. D.; Kim, J.-S.; Chin, C.; Jay Guo, L. Nanoimprint Lithography Based Approach for the Fabrication of Large-Area, Uniformly-Oriented Plasmonic Arrays. *Adv. Mater.* **2008**, *20* (6), 1129–1134.
(38) Boltasseva, A. Plasmonic Components Fabrication via Nanoimprint. *J. Opt. A: Pure Appl. Opt.* **2009**, *11* (11), 114001.
(39) Pedersen, R. H.; Boltasseva, A.; Johansen, D. M.; Nielsen, T.; Jørgensen, K. B.; Leosson, K.; Østergaard, J. E.; Kristensen, A. Nanoimprinted Reflecting Gratings for Long-Range Surface Plasmon Polaritons. *Microelectron. Eng.* **2007**, *84* (5-8), 895–898.
(40) Fernandez-Cuesta, I.; Nielsen, R. B.; Boltasseva, A.; Borrisé, X.; Pérez-Murano, F.; Kristensen, A. V-Groove Plasmonic Waveguides Fabricated by Nanoimprint Lithography. *J. Vac. Sci. Technol. B Microelectron. Nanometer Struct. Process. Meas. Phenom.* **2007**, *25* (6), 2649.
(41) Nielsen, R. B.; Fernandez-Cuesta, I.; Boltasseva, A.; Volkov, V. S.; Bozhevolnyi, S. I.; Klukowska, A.; Kristensen, A. Channel Plasmon Polariton Propagation in Nanoimprinted V-Groove Waveguides. *Opt. Lett.* **2008**, *33* (23), 2800–2802.
(42) Wu, W.; Yu, Z.; Wang, S.-Y.; Stanley Williams, R.; Liu, Y.; Sun, C.; Zhang, X.; Kim, E.; Ron Shen, Y.; Fang, N. X. Midinfrared Metamaterials Fabricated by Nanoimprint Lithography. *Appl. Phys. Lett.* **2007**, *90* (6), 063107.
(43) Wu, W.; Kim, E.; Ponizovskaya, E.; Liu, Y.; Yu, Z.; Fang, N.; Shen, Y. R.; Bratkovsky, A. M.; Tong, W.; Sun, C.; Zhang, X.; -Y. Wang, S.; Williams, R. S. Optical Metamaterials at near and Mid-IR Range Fabricated by Nanoimprint Lithography. *Appl. Phys. A: Mater. Sci. Process.* **2007**, *87* (2), 143–150.
(44) Yao, Y.; Liu, H.; Wang, Y.; Li, Y.; Song, B.; Wang, R. P.; Povinelli, M. L.; Wu, W. Nanoimprint-Defined, Large-Area Meta-Surfaces for Unidirectional Optical Transmission with Superior Extinction in the Visible-to-Infrared Range. *Opt. Express* **2016**, *24* (14), 15362–15372.
(45) Bergmair, I.; Dastmalchi, B.; Bergmair, M.; Saeed, A.; Hilber, W.; Hesser, G.; Helgert, C.; Pshenay-Severin, E.; Pertsch, T.; Kley, E. B.; Hübner, U.; Shen, N. H.; Penciu, R.; Kafesaki, M.; Soukoulis, C. M.; Hingerl, K.; Muehlberger, M.; Schoeftner, R. Single and Multilayer Metamaterials Fabricated by Nanoimprint Lithography. *Nanotechnology* **2011**, *22* (32), 325301.
(46) Cattoni, A.; Ghenuche, P.; Haghiri-Gosnet, A.-M.; Decanini, D.; Chen, J.; Pelouard, J.-L.; Collin, S. λ^3/1000 Plasmonic Nanocavities for Biosensing Fabricated by Soft UV Nanoimprint Lithography.

Nano Lett. **2011**, *11* (9), 3557–3563.
(47) Yao, J.; Le, A.-P.; Gray, S. K.; Moore, J. S.; Rogers, J. A.; Nuzzo, R. G. Functional Nanostructured Plasmonic Materials. *Adv. Mater.* **2010**, *22* (10), 1102–1110.
(48) Lee, S.-W.; Lee, K.-S.; Ahn, J.; Lee, J.-J.; Kim, M.-G.; Shin, Y.-B. Highly Sensitive Biosensing Using Arrays of Plasmonic Au Nanodisks Realized by Nanoimprint Lithography. *ACS Nano* **2011**, *5* (2), 897–904.
(49) Varghese, L. T.; Fan, L.; Xuan, Y.; Tansarawiput, C.; Kim, S.; Qi, M. Resistless Nanoimprinting in Metal for Plasmonic Nanostructures. *Small* **2013**, *9* (22), 3778–3783.
(50) Liang, C.-C.; Liao, M.-Y.; Chen, W.-Y.; Cheng, T.-C.; Chang, W.-H.; Lin, C.-H. Plasmonic Metallic Nanostructures by Direct Nanoimprinting of Gold Nanoparticles. *Opt. Express* **2011**, *19* (5), 4768–4776.
(51) Chen, W.; Tymchenko, M.; Gopalan, P.; Ye, X.; Wu, Y.; Zhang, M.; Murray, C. B.; Alu, A.; Kagan, C. R. Large-Area Nanoimprinted Colloidal Au Nanocrystal-Based Nanoantennas for Ultrathin Polarizing Plasmonic Metasurfaces. *Nano Lett.* **2015**, *15* (8), 5254–5260.
(52) Chen, W.; Wu, G.; Zhang, M.; Greybush, N. J.; Howard-Jennings, J. P.; Song, N.; Scott Stinner, F.; Yang, S.; Kagan, C. R. Angle-Independent Optical Moisture Sensors Based on Hydrogel-Coated Plasmonic Lattice Arrays. *ACS Applied Nano Materials* **2018**, *1* (3), 1430–1437.
(53) Park, S. J.; Ok, J. G.; Park, H. J.; Lee, K.-T.; Lee, J. H.; Kim, J. D.; Cho, E.; Baac, H. W.; Kang, S.; Jay Guo, L.; John Hart, A. Modulation of the Effective Density and Refractive Index of Carbon Nanotube Forests via Nanoimprint Lithography. *Carbon N. Y.* **2018**, *129*, 8–14.
(54) Taylor, J. H.; Yates, H. W. Atmospheric Transmission in the Infrared. *J. Opt. Soc. Am.* **1957**, *47* (3), 223.
(55) Yates, H. W.; Taylor, J. H. *Infrared Transmission of the Atmosphere*; **1960**.
(56) Werle, P.; Slemr, F.; Maurer, K.; Kormann, R.; Mücke, R.; Jänker, B. Near- and Mid-Infrared Laser-Optical Sensors for Gas Analysis. *Opt. Lasers Eng.* **2002**, *37* (2-3), 101–114.
(57) Richter, D.; Erdelyi, M.; Curl, R. F.; Tittel, F. K.; Oppenheimer, C.; Duffell, H. J.; Burton, M. Field Measurements of Volcanic Gases Using Tunable Diode Laser Based Mid-Infrared and Fourier Transform Infrared Spectrometers. *Opt. Lasers Eng.* **2002**, *37* (2-3), 171–186.
(58) Rayleigh, Lord. LIII. Remarks upon the Law of Complete Radiation. *The London, Edinburgh, and Dublin Philosophical Magazine and Journal of Science* **1900**, *49* (301), 539–540.
(59) Zhao, Y. Dynamic Shadowing Growth and Its Energy Applications. *Front. Energy Res*. **2014**, *2*, 38.
(60) Madou, M. J. Fundamentals of Microfabrication and Nanotechnology, Three-Volume Set. *CRC Press* **2018**.
(61) Tyagi, P.; Bassik, N.; Leong, T. G.; Cho, J.-H.; Benson, B. R.; Gracias, D. H. Self-Assembly Based on Chromium/Copper Bilayers. *J. Microelectromech. Syst*. **2009**, *18* (4) 784–791.
(62) Hagemann, H. J.; Gudat, W.; Kunz, C. Optical Constants from the Far Infrared to the X-Ray Region: Mg, Al, Cu, Ag, Au, Bi, C, and Al_2O_3. *J. Opt. Soc. Am.* **1975**, *65*, 742-744.
(63) Dodge, M. J. Refractive Properties of Magnesium Fluoride. *Appl. Opt*. **1984**, *23* (12) 1980-1985.
(64) Arbabi, A.; Briggs, R. M.; Horie, Y.; Bagheri, M.; Faraon, A. Efficient Dielectric Metasurface Collimating Lenses for Mid-Infrared Quantum Cascade Lasers. *Opt. Express* **2015**, *23* (26), 33310–33317.
(65) Yu, N.; Genevet, P.; Kats, M. A.; Aieta, F.; -P. Tetienne, J.; Capasso, F.; Gaburro, Z. Light Propagation with Phase Discontinuities: Generalized Laws of Reflection and Refraction. *Science*. **2011**, *334* (6054), 333–337.
(66) Li, S.-Q.; Song, W.; Ye, M.; Crozier, K. B. Generalized Method of Images and Reflective Color Generation from Ultrathin Multipole Resonators. *ACS Photonics*. **2018**, *5* (6), 2374–2383.
(67) Ye, M.; Li, S.-Q.; Gao, Y.; Crozier, K. B. Long-Wave Infrared Magnetic Mirror Based on Mie Resonators on Conductive Substrate. *Opt. Express* **2020**, *28* (2), 1472–1491.
(68) Ding, F.; Yang, Y.; Deshpande, R. A.; Bozhevolnyi, S. I. A Review of Gap-Surface Plasmon Metasurfaces: Fundamentals and Applications. *Nanophotonics*. **2018**, *7* (6) 1129–1156.
(69) Gramotnev, D. K.; Pors, A.; Willatzen, M.; Bozhevolnyi, S. I. Gap-Plasmon Nanoantennas and

Bowtie Resonators. *Phys. Rev. B*. **2012**, *85* (4), 045434.
(70) Novotny, L. Effective Wavelength Scaling for Optical Antennas. *Phys. Rev. Lett*. **2007**, *98* (26), 266802.
(71) Li, H. H. Refractive Index of Alkaline Earth Halides and Its Wavelength and Temperature Derivatives. *J. Phys. Chem. Ref. Data*. **1980**, *9* (1) 161–290.
(72) Lucas, J.; Smektala, F.; Adam, J. L. Fluorine in Optics. *J. Fluor. Chem.* **2002**, *114* (2) 113–118.
(73) Li, S.-Q.; Zhou, W.; Bruce Buchholz, D.; Ketterson, J. B.; Ocola, L. E.; Sakoda, K.; Chang, R. P. H. Ultra-Sharp Plasmonic Resonances from Monopole Optical Nanoantenna Phased Arrays. *Appl. Phys. Lett*. **2014**, *104* (23), 231101.
(74) Li, S. Q.; Guo, P.; Zhang, L.; Zhou, W.; Odom, T. W.; Seideman, T.; Ketterson, J. B.; Chang, R. P. H. Infrared Plasmonics with Indium–Tin-Oxide Nanorod Arrays. *ACS Nano*. **2011**, *5* (11), 9161–9170.

TOC figure

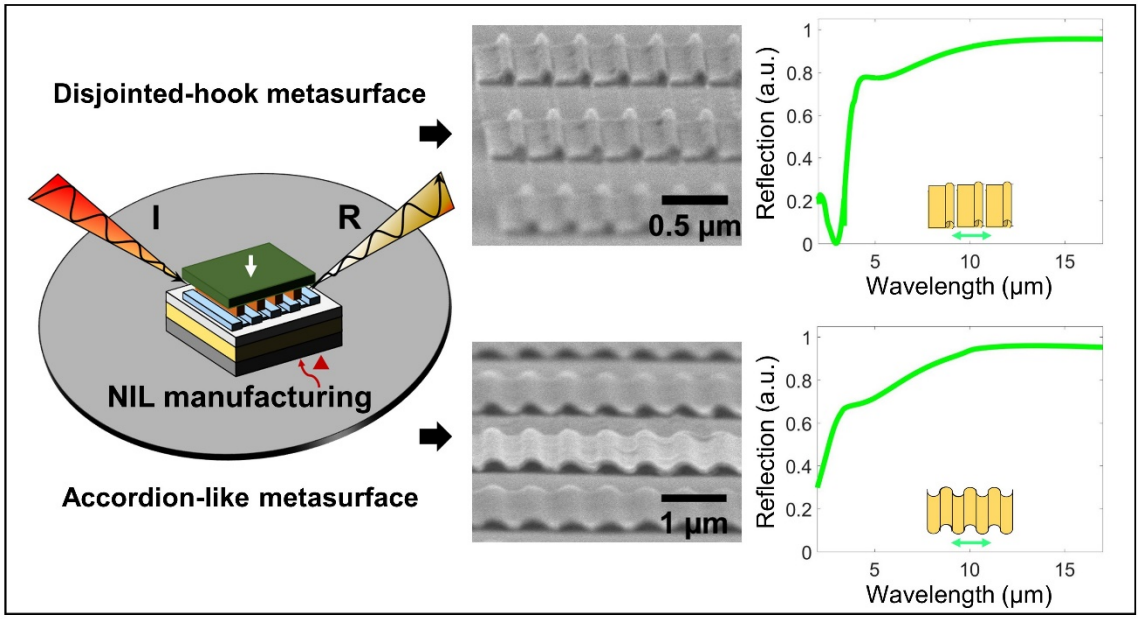

Supporting Information

For

Large-Area Arrays of Quasi-3D Au Nanostructures for Polarization-Selective Mid-Infrared Metasurfaces

Vivek Nagal[1]; Tengfei Li[2]; Jacob B. Khurgin[2,]; David H. Gracias[1,*] (dgracias@jhu.edu)*

[1]Department of Chemical and Biomolecular Engineering and [2]Department of Electrical Engineering, Johns Hopkins University, Baltimore, Maryland 21218, United States

*Corresponding Author email: dgracias@jhu.edu; jakek@jhu.edu

Table of Contents

1. Geometric designs for DHM and ALM

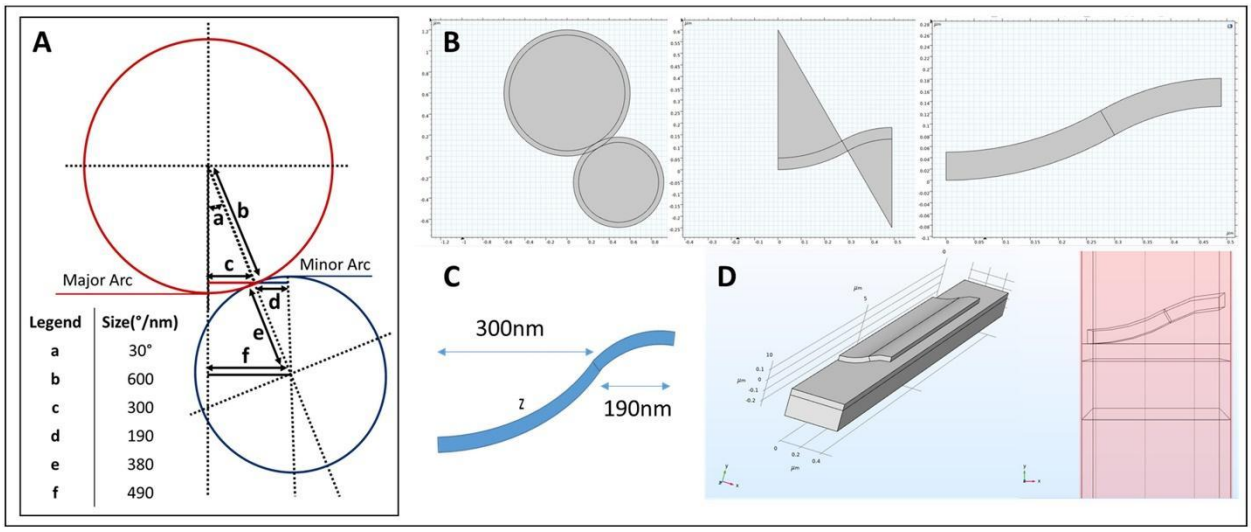

Figure S1: (a) Basic geometric mathematical shape description illustrating the modelling of the DHM as a combination of two arcs from different circles. **(b)** Cross sectional derivation to the final unit cell shape in COMSOL. **(c)** Schematic of unit cell. **(d)** Unit cell as seen in COMSOL with underlying dielectric and metal layers

In order to effectively capture the geometry of fabricated metasurfaces, we tried different unit cell models. Here, we show the layout for the setup that gave the best agreement with our experimental findings. The DHM was modelled as shown in **Fig. S1** as a combination of two arcs from circles of different radius to capture the asymmetry along the width. Similarly, for the ALM unit cell, as described in **Fig. S2**, we used 2 smaller circles for the sides and a larger circle for the central bulge, to generate the resulting cell resembling our SEM micrographs.

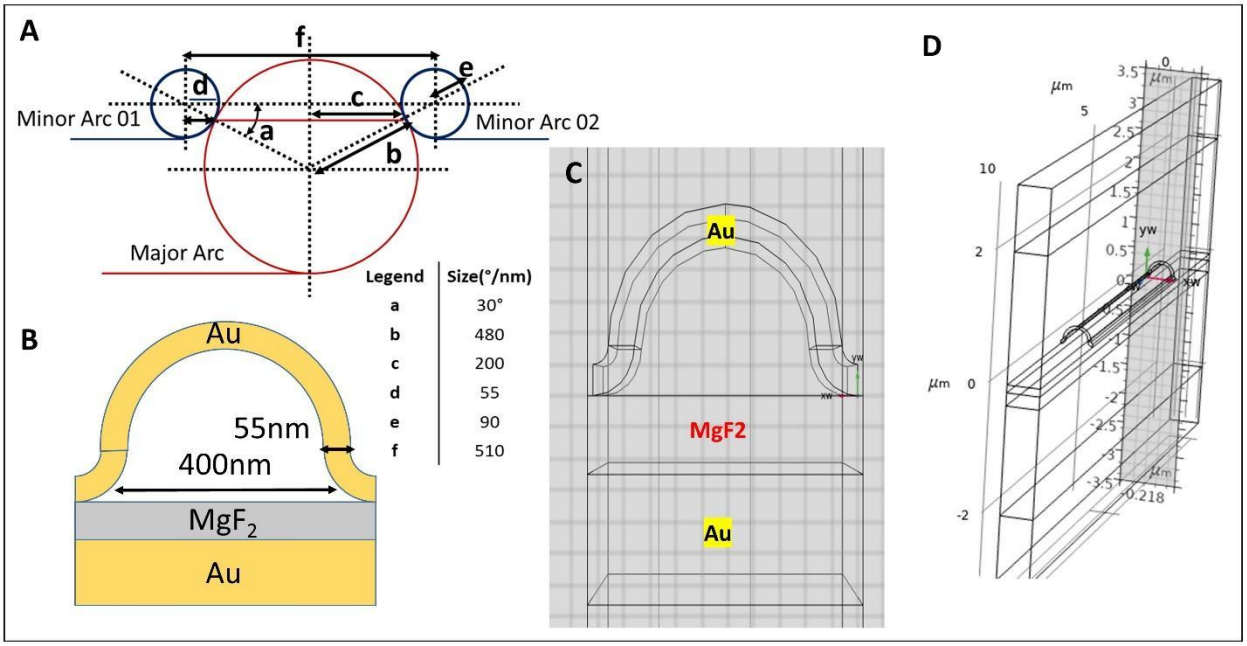

Figure S2: (a) Basic mathematical shape description using geometry concepts illustrating modelling of the ALM as a combination of 3 arcs from different circles; **(b)** Side view schematic of unit cell **(c, d)** Unit cell as seen in COMSOL with underlying dielectric and metal layers.

2. ImageJ analysis for dimensional characterization

In order to quantify the dimensions of our fabricated antennas, we analyzed the SEM micrographs in ImageJ. The exported image was first converted to 8-bit type, and appropriate upper and lower threshold values were set to segment the grayscale image into the features of interest and background. The resulting extracted image is shown in **Fig. S3** (A (i, ii)), for the source image in panel C (ii) which is a top view of the DHM. The scale was set by measuring the pixel count of the scale bar originally in the SEM. This forms the basis of all measurements in the image. The 'analyze particles' tool was identify each antenna as a 'particle' using shape description parameter cut offs based on circularity and aspect ratio. By collecting data on this parameter along with the center of mass coordinates, bounding rectangle coordinates and perimeter, we were able to tabulate the average periodicity, length and width of our antennas, averaged over 20 [source figure: C (i)] and 80 [source figure C (ii)] antennas as shown in panel B.

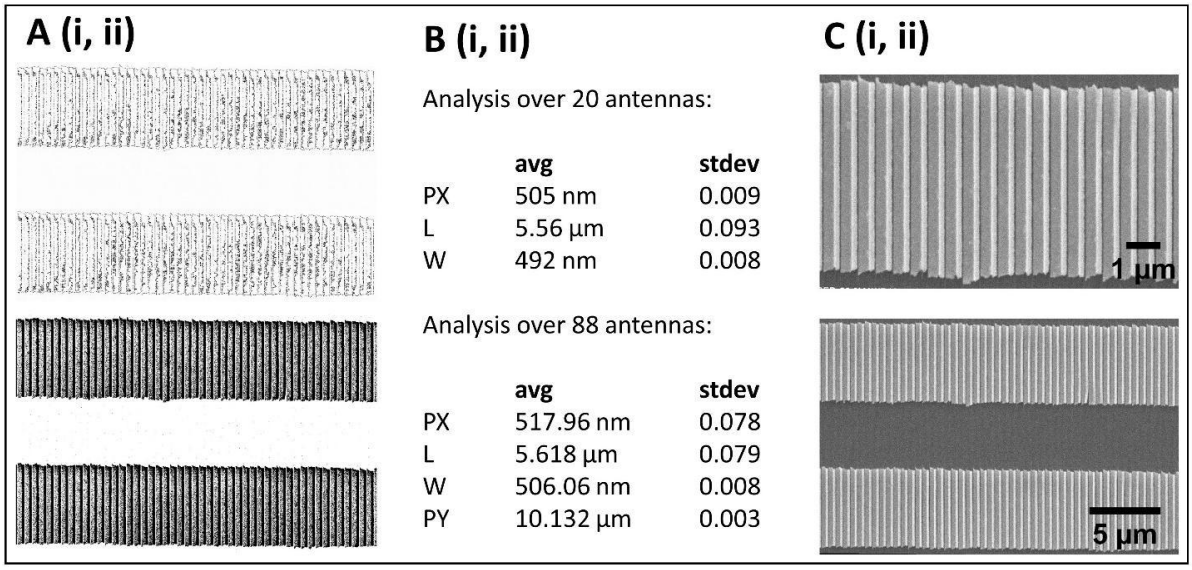

Figure S3: (a) Grayscale extraction and identification of individual antennas in DHM from their SEM counterparts in **(c)** Top view SEM micrographs used for ImageJ analysis, and **(b)** resulting dimensions obtained by performing two different sets of data averaging.

3. The dielectric constant of different widely used metals

In the research of metamaterials and metasurfaces, the most widely used metal is gold, especially in the traditional optical region (400-700nm), compared to other metals, such as silver. In our study, our focus was the mid-IR (2μm-10μm) wavelength range due to potential applications in defense and remote sensing.

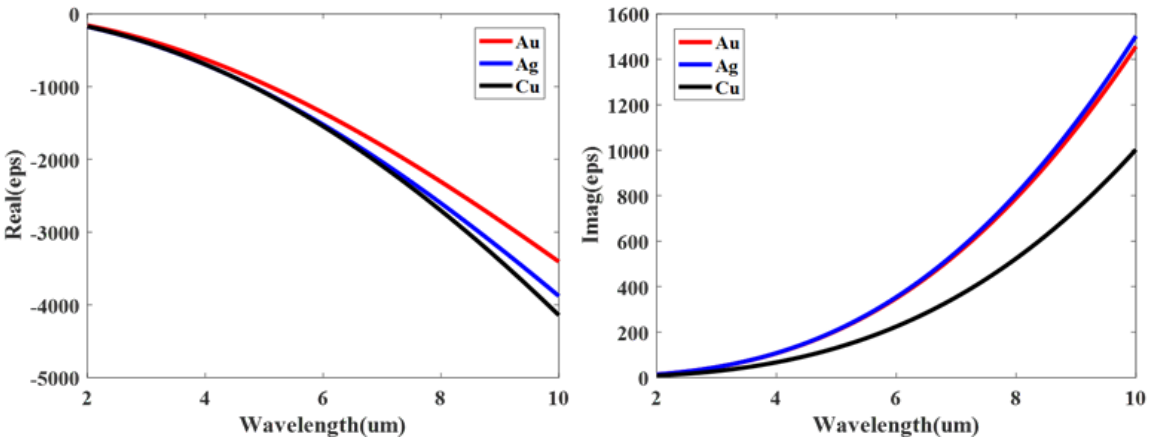

Figure S4: (a) The real and **(b)** imaginary part of the dielectric constant of gold silver and copper in the mid-IR wavelength region (2-10μm)

4. Comparison of overlapping fano resonances

We simulated the electric field intensity distributions at the wavelengths 3.37, 5.08 and 10.13 μm, where we observed sharp low intensity features in the spectrum indicating fano resonances. For both DHM and ALM, these resonances occur at the same wavelengths making them independent of the antenna dimensions or topography. Their sharp nature is reaffirmed by the bright high intensity hot spots in the **Fig. S5**. The distribution is symmetric for ALM and asymmetric for DHM and the intensity is slightly higher for the ALM case than the DHM. When the polarization is along the length, fano resonances occur due to the coupling between the broad plasmonic resonance and the narrow slab waveguide mode.[1] The latter implies the waveguide between the top antenna array and bottom Au layer. They can be excited for width polarization too when the coupling is between the grating and waveguide mode.

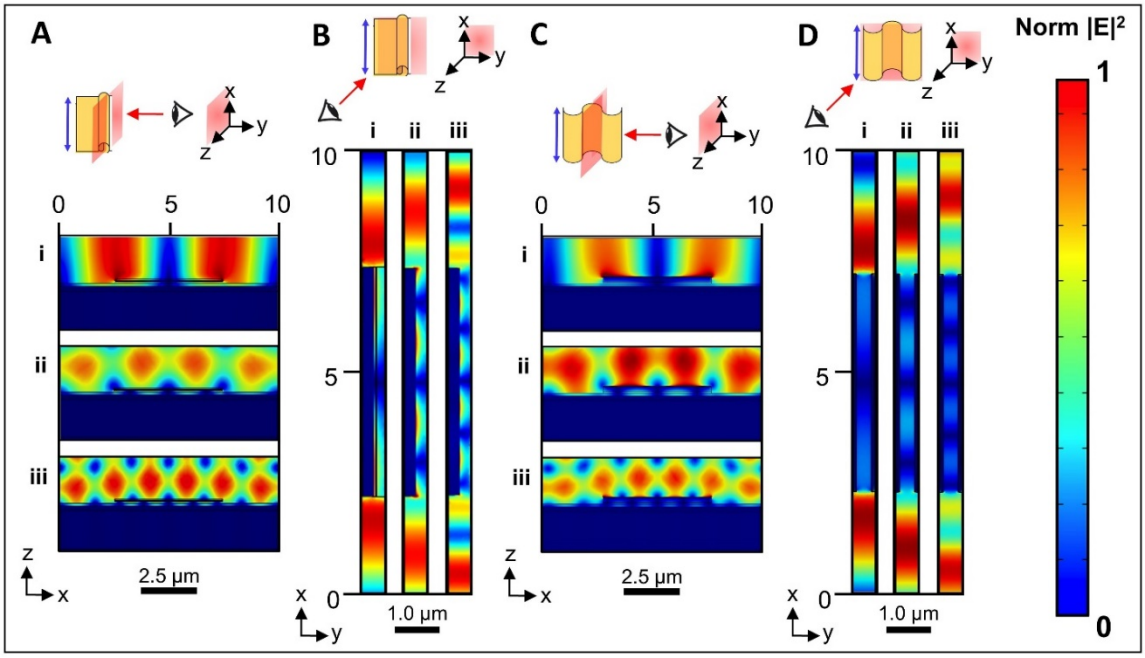

Figure S5: Electric field |E| distributions **(A)** around the DHM unit cell: **(i-iii)** representing the fano resonances observed in reflection response for increasingly blue wavelengths from top **(i)** to bottom **(iii)** as viewed from the side projection in the x-z plane; **(B) (i-iii)** as viewed from the top projection in x-y plane for same wavelengths respectively; **(C)** The corresponding fano resonances for ALM for same plane of projection as **(A)**; and **(D)** same as the projections as outlined in **(B)**. Top inset schematics indicate where the plane of interest meets the antenna for said cases.

5. Comparison of polarization selectivity for 4 different cases

In order to validate the conclusion from main text in Fig. 9 regarding the polarization selectivity of our metasurfaces when incident polarization is along the width, we analyzed the field distribution at the wavelength 4.23 μm in **Fig. S6** where we see a vivid pit in the reflection spectra of unpatterned rectangular gold cantilevers, seen in Fig. 9(F). Although the pit for DHM is seen at a smaller wavelength as seen in Fig. 9(G), we decided to compare the 4 cases at the same wavelength, since it doesn't alter our conclusion. The absence of any hot spots in panels A and D compared to significant activity in panels B and C confirm that geometry plays a key factor in eventual selectivity towards incoming light. The distribution of hot spots in DHM in panel C are again in coherence with its asymmetric topography.

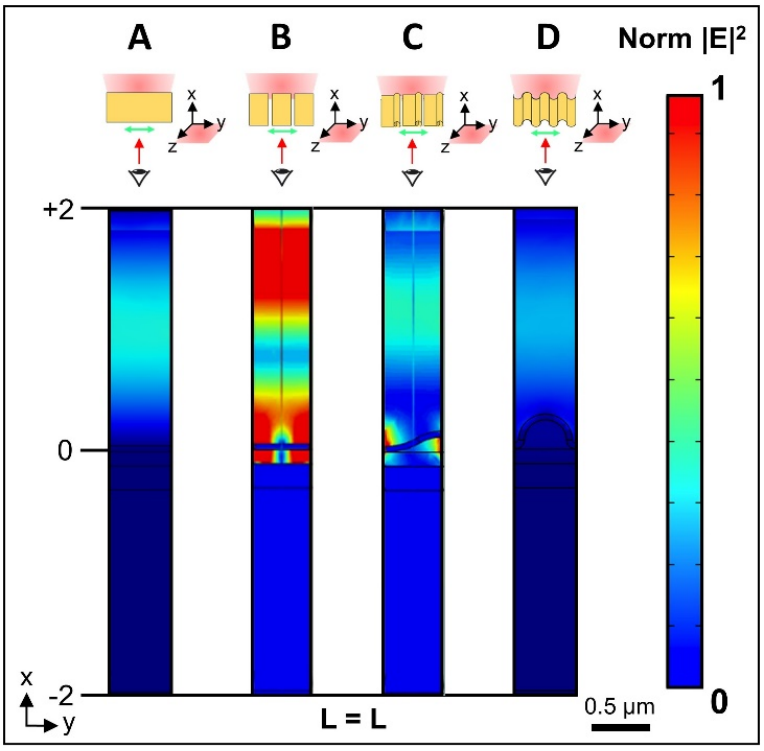

Figure S6: Electric field |E| distributions when the polarization is along the width of the antenna as indicated by the inset schematics for the 4 different cases explores in Fig. 8 of main text. **(A)** Continuous single gold strip periodic in y-axis; **(B)** unpatterned rectangular gold cantilevers with perfectly flat and smooth topography periodic in both x and y axis; **(C)** DHM and **(D)** ALM. Here we show the cross sectional view projections in y-z plane taken at one end of the antenna [L = 0 or L = L] for the wavelength where a dip in reflection is observed.

REFERENCES

(1) Luk'yanchuk, B.; Zheludev, N. I.; Maier, S. A.; Halas, N. J.; Nordlander, P.; Giessen, H.; Chong, C. T. The Fano Resonance in Plasmonic Nanostructures and Metamaterials. *Nat. Mater*. **2010**, *9* (9), 707–715.